A photovoltaic window with sun-tracking shading elements towards maximum power generation and non-glare daylighting

Gao, Yuan; Dong, Jianfei; Isabella, Olindo; Santbergen, Rudi; Tan, Hairen; Zeman, Miro; Zhang, Guo Qi

DOI
10.1016/j.apenergy.2018.07.015

Publication date
2018

Document Version
Accepted author manuscript

Published in
Applied Energy

A Photovoltaic Window with Sun-Tracking Shading Elements towards Maximum Power Generation and Non-Glare Daylighting

Yuan Gao[a,b,c,*], Jianfei Dong[d,b], Olindo Isabella[a], Rudi Santbergen[a], Miro Zeman[a,*], Guoqi Zhang[e,*]

[a] *PVMD/DIMES, Delft University of Technology, Delft, The Netherlands*
[b] *Beijing Research Center, Delft University of Technology, Beijing, China*
[c] *Changzhou Institute of Technology Research for Solid State Lighting, Changzhou, China*
[d] *Suzhou Institute of Biomedical Engineering and Technology, Chinese Academy of Sciences, Suzhou, China*
[e] *Department of Microelectronics, Delft University of Technology, Delft, The Netherlands*

Abstract

Vertical space bears great potential of solar energy especially for congested urban areas, where photovoltaic (PV) windows in high-rise buildings can contribute to both power generation and daylight harvest. Previous studies on sun-tracking PV windows strayed into the trade-off between tracking performance and mutual shading, failing to achieve the maximum energy generation. Here we first mathematically prove that one-degree-of-freedom (DOF) and two-DOF sun tracking are not able to gain either maximum power generation or non-glare daylighting under reasonable assumptions. Then we derive the optimum rotation angles of the variable-pivot-three-degree-of-freedom (VP-3-DOF) sun-tracking elements and demonstrate that the optimum VP-3-DOF sun tracking can achieve the aforementioned goals. Despite the strict model in this study, the same performance can be achieved by the optimum one-DOF sun tracking with extended PV slats and particular design of cell layout, requiring less complicated mechanical structures. Simulation results show that the annual energy generation and average module efficiency are improved respectively by 27.40% and 19.17%

[☆] See the supplementary document for more information.

[*] Corresponding author

Email addresses: Y.Gao-1@tudelft.nl (Yuan Gao), M.Zeman@tudelft.nl (Miro Zeman), G.Q.Zhang@tudelft.nl (Guoqi Zhang)

via the optimum VP-3-DOF sun tracking over the conventional perpendicular sun tracking. The optimum VP-3-DOF sun tracking is also demonstrated to be applicable to horizontal PV windows, as those applied in the sun roof of a glass greenhouse.

Keywords: photovoltaics, partial shading effects, sun-tracking methods, BIPV, solar energy

2018 MSC: 00-00, 00-00

---

1. Introduction

1.1. Motivation

A photovoltaic (PV) window is a daylight-management apparatus with photovoltaic solar cells, modules, or systems embedded on, in, or around a window [1, 2, 3, 4]. PV windows take full advantage of vertical space in congested urban areas, where available horizontal lands are scarce, and local energy consumptions are tremendous. To evaluate the equivalent horizontal area (EHA) of available vertical surfaces, we define $R_{v/h}$ as the ratio of the annual solar energy received on the sunward (e.g. equator-facing for temperate zones) vertical unit area to that received on the horizontal unit area, i.e.,

$$R_{v/h} = \frac{\int G_{v,global}(t)\,dt}{\int G_{h,global}(t)\,dt}, \tag{1}$$

where $G_{v,global}(t)$ indicates the global irradiance on a sunward vertical plane; and $G_{h,global}(t)$ indicates the global irradiance on a horizontal plane. The integration time here is an entire year (365 days). According to reliable climate data [5], the calculated value of $R_{v/h}$ for Shanghai is 0.8717. More specifically, the EHA of the highest skyscraper (632 m) in Shanghai equals to the area of 3.5 standard football fields, which occupy 15.6-fold horizontal areas as the building does (see Supplementary Note 1). $R_{v/h}$ for nine selected cities is calculated and shown in Table 1. Considering all the urban high-rise buildings around the world, vertical area holds enormous potential for the utilization of solar energy, especially the window area, which is relatively large in modern buildings.

Table 1: $R_{v/h}$ of nine selected cities around the world

City	$R_{v/h}$
Shanghai	0.8717
New York City	0.9128
Tokyo	0.9345
Beijing	0.9629
London	1.0233
Los Angeles	0.7799
Toronto	0.9289
Paris	0.9669
Berlin	1.0181

Besides the potential of power generation, PV windows also contribute to the energy balance of modern architectural environment via daylight control and heat insulation.

1.2. Previous studies

The nature of PV windows is to manipulate photons in order to turn incident light partially into electricity and partially into transmitted light. Most reported approaches are implemented by integrating transparent, semi-transparent, regionally transparent PV, or light-directed materials with window glazing. Regionally transparent PV windows can be simply formed by distributing available opaque solar cells discretely onto window glasses [6, 7], resulting in undesired partially-blocked view and spotted shadows. By shrinking the size of opaque solar cells [8, 9, 10, 11] or punching small holes on the opaque surface [12], the visual effects are possibly improved, however, at the cost of complicating the manufacturing process. Unlike opaque PV materials, semi-transparent solar cells reveal uniform transmittance with colored [13, 14, 15, 16, 17, 18] or neutrally-colored [19, 20, 21, 22, 23, 24] appearance. Since photons are selectively transmitted, semi-transparent photovoltaic (STPV) materials [25] present lower efficiency comparing with the corresponding opaque materials. To pursue crystal clear appearance, fully transparent solar cells [26, 27, 28] are developed by selectively harvesting near-infrared (NIR) and ultraviolet (UV) light, leading to lower efficiency than STPV. Another approach is utilizing PV and luminescent solar concentrators (LSCs) [29, 30, 31, 32, 33], which also suffer from the low-efficiency problem. Moreover, none of the approaches mentioned above can enable glare protection from direct sunlight.

To overcome the obstacles faced by passive approaches, e.g. low efficiency and sunlight glare, sun-tracking PV windows, which integrated PV materials with active window treatments (e.g. blinds, shutters, etc.), have been designed and investigated by many authors. PV blinds with one degree-of-freedom (DOF) slats are mostly reported due to easy-access experimental setups. Luo et al. conducted a comparative study of PV blinds by varying the spacing between adjacent blinds (2.5 cm, 3.5 cm, and 4.5 cm) and by varying the slat angle (30°, 45°, and 60°) [34]. However, the analysis was focusing on the thermal performance of the PV blinds, in stead of the PV power generation. Hu et al. compared three types of building integrated photovoltaic (BIPV) Trombe wall system in terms of their annual performance [35, 36]. Comparing with existing PV Trombe walls, the type with PV blinds showed 45% higher electricity saving. Optimum slat angles were selected from six fixed angels (from 0° to 75° in 15° steps intervals) over three seasons and time of the day. But here PV blinds were integrated with walls instead of windows, failing to contribute to the daylighting of indoor environment. Hong et al. mentioned that the partial shading effect caused by the slats had a nonlinear effect on the amount of electricity generation [37]. The width of the PV panel was taken as one of the variables. Particularly, as the width of PV panel increased, the amount of electricity generation per unit area and the saving-to-investment ratio at year 25 decreased, but the net present value at year 25 tended to increase. However, the slope of the PV blind′s slat was not considered as the variable at the same time during the optimization. In order to estimate the techno-economic performance of the building integrated photovoltaic blind, Park et al. developed a four node based finite element model (FEM_{4-node}) [38]. Later, Koo et al. improved this model by proposing a nine-node-based finite element model (FEM_{9-node}) [39]. The model claimed to have better prediction accuracy (3.55%) and standard deviation (2.93%) than the previous one. However, the partial shading effect caused by slats was hard to be simulated precisely considering dynamic slopes and shadows. Most of the cases mentioned above and some other research [40, 41, 42, 43] share a common problem that the optimal tilt angle was reported as a static value, instead of a function of the solar position. Only one study conducted by Hong et al. proposed a dynamic sun-tracking method, which can avoid shadows on the slats of the bi-directional PV blind [44]. But it neither theocratically analyzed the input power, nor derived the optimal tilt angle by the function of the solar position.

Two-DOF sun-tracking PV shading devices have also been studied based on a prototype of an adaptive solar envelope (ASE) at the ETH House of Natural Resources [45]. Hofer et al. tackled the partial shading problem by adjusting the size of PV panel on the square and the distance between squares, without considering to use other sun-tracking method [46]. Jayathissa et al. chose the optimal sun-tracking method by exploring all possible dynamic PV orientations [47]. However, for simplicity, all PV panels moved simultaneously with discrete angles (15°). Therefore, it can not achieve a continuous sun tracking according to the solar position.

1.3. Objectives

A common misconception is that BIPV sun tracking is to orient the PV surface perpendicular to the sun rays. This misconception stems from the sun-tracking method commonly found in conventional PV power stations, where sun trackers (or solar trackers) are used to orient flat PV panels towards the sun in order to increase the energy collection. During daylight hours, the PV panels are kept in an optimum position perpendicular to the direction of the solar radiation [48]. Theoretical explanation of ubiquitous perpendicular-sun-tracking methods resides in the basic model of the global irradiance on a tilt plane ($G_{t,global}$) [49], i.e.,

$$G_{t,global} = I_e^{dir} \cos\gamma + G_{h,d}R_d + G_{t,ground}, \tag{2}$$

where I_e^{dir} is the direct normal (or direct beam) irradiance (DNI) of the sunlight; γ is the angle between the PV surface normal and the incident direction of the sunlight; $G_{h,d}$ is the diffuse horizontal irradiance; R_d is the diffuse transposition factor; $G_{t,ground}$ is the ground-reflected irradiance. The product $I_e^{dir} \cos\gamma$ represents the direct irradiance on the tilt plane, i.e. $G_{t,beam}$, which is a dominant component contributing more than 90% of the global irradiance in a cloudless day [50]. The other two components, diffuse ($G_{t,d} = G_{h,d}R_d$) and ground-reflected irradiance, contribute a small proportion to the clear-sky $G_{t,global}$, and vary with the orientation of the plane. If we ignore the variations of those two components caused by the orientation and take such components as orientation-independent constants because of their small contribution, we can conclude that the maximum $G_{t,global}$ is achieved when γ equals to zero, i.e. the PV surface is perpendicular to the incident sun rays. The maximum $G_{t,global}$ leads to the maximum incident energy per unit time, i.e. the maximum input power P_{in}, because the direct-beam-illuminated PV area S_b remains as a constant; i.e.

$$P_{in} = G_{t,global}S_b. \tag{3}$$

However, the perpendicular-sun-tracking method is not necessarily applicable to BIPV due to complicated building environment and multiple sun-tracking purposes. Comparing with conventional sun-tracking PVs, building integrated sun-tracking PVs make a profound difference because S_b shrinks when shadows appear on the PV surface caused by adjacent elements. In this circumstance, the product of a maximum $G_{t,global}$ with a reduced S_b cannot guarantee a maximum P_{in} any more. The shadows on the PV surface not only lead to a diminished S_b, but also result in PV partial shading problems, which affect the PV performance, especially the module efficiency η_m. η_m drops dramatically when uneven shadows are found on series-connected solar cells. PV module performs the best when no shadow casts upon it. To maximize P_{out} at a given time, a straightforward way is keeping the PV surface towards the optimal orientation, where it receives the maximum P_{in}; and no shadow appears on it, resulting in the maximum η_m (Eq. 4). Therefore, one of the purposes of sun tracking is to preserve the maximum P_{out} at every tracking moment, so that the PV module generates the maximum energy E, which is the integral of P_{out} over a certain period of time t (Eq. 5).

$$P_{out} = P_{in}\eta_m. \tag{4}$$

$$E = \int P_{out}(t)\, dt. \tag{5}$$

As to BIPV, sun tracking is not only aiming at the maximum E, but also the capability to fulfill building functions. For window treatments, two main functions are daylighting and glare protection. In a nutshell, the objectives of building integrated solar tracking for PV window are to receive the maximum P_{in}, to avoid shadows on the PV surface, and to enable daylighting without glare. This work focuses on the solutions to meet these objectives.

In this work, several models were first built up for simulating the performance of PV shading elements under partial shading conditions. Those models include solar irradiance and shadows on the rotated PV surface, solar cells, PV modules, equivalent irradiance, and glare. Then we investigated one-DOF, two-DOF, and three-DOF sun tracking and derived corresponding rotation angles. We summarized simulation results of four sun-tracking methods using irradiance data of Shanghai. Simulations of the optimum variable-pivot-three-degree-of-freedom (VP-3-DOF) and perpendicular sun tracking were conducted using irradiance data of nine big cities around the world. Finally, optimal cell patterns of one-DOF sun tracking were discussed; and an extended application of VP-3-DOF sun tracking in horizontal windows was introduced and demonstrated.

2. Methodology

Unlike the method of case study in most aforementioned literatures, in this study, a general theory of BIPV sun tracking method is developed based on modeling and simulation. Simplifications and assumptions are properly applied to the models and simulations to achieve general sun-tracking solutions in complex architectural environment. The solar irradiance model is built based on typical conditions of building windows and window treatments. The shadow position on PV shading elements is derived from basic three-dimensional rotation matrices using the knowledge of solid analytical geometry. Shadows on shading elements are simulated and observed by SketchUp [51]. Taking the partial shading effects into consideration, the annual energy generation is then calculated in the simulation model built by MATALB SimuLink, using the climate database from Meteonorm [5]. Point-in-time glare is simulated in the Rhinoceros model of a reference room by Grasshopper [52].

2.1. Model of solar irradiance on PV shading elements

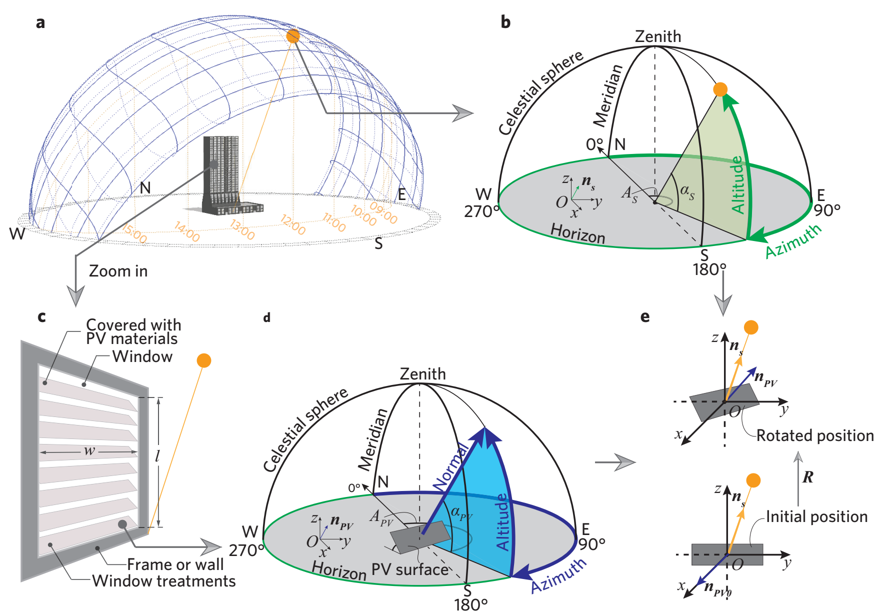

Figure 1: **Definitions for the irradiance model.**

Firstly, an equator-facing window in the sunward side of a high-rise building is defined, which is rarely shaded by surrounding objects from the sun (Fig. 1a).

We only consider the buildings located in the temperate zone (between 23.5° and 66.5° for both north and south latitude) to ensure the sun stays the same side of the building during the PV-functioning hours for an entire year. Usually, the solar position is defined by the solar altitude α_s and the solar azimuth A_s in the horizontal coordinate system. Here, we denote the solar position by a unit vector $\boldsymbol{n_s}(x_s, y_s, z_s)$ in corresponding Cartesian coordinate system (Fig. 1b). Eq. 6 transforms the spherical coordinates into the Cartesian coordinates.

$$\boldsymbol{n_s} = \begin{bmatrix} x_s \\ y_s \\ z_s \end{bmatrix} = \begin{bmatrix} -\cos\alpha_s \cos A_s \\ \cos\alpha_s \sin A_s \\ \sin\alpha_s \end{bmatrix}. \quad (6)$$

Analogously, the orientation of the PV surface on the shading element is denoted by the altitude α_{PV} and the azimuth A_{PV} of the normal of the PV surface in the horizontal coordinate system, and $\boldsymbol{n_{PV}}(x_n, y_n, z_n)$ in the Cartesian coordinate system (Fig. 1d). By the aforementioned definitions, we succeed in including $\boldsymbol{n_{PV}}$ and $\boldsymbol{n_s}$ in the same three-dimensional Cartesian coordinate system (Fig. 1e). Since $\boldsymbol{n_{PV}}$ only indicates the orientation of the PV surface instead of the exact position of the shading element, here we define the initial position of the shading element (a rectangular PV module) as a vertical plane facing equator ($\boldsymbol{n_{PV0}}(1, 0, 0)$), and let one side of the rectangle be parallel with the horizontal plane. An arbitrary position can be achieved from the initial position by a series of rotations, which is mathematically expressed as a rotation matrix, denoted as $\boldsymbol{R}$ (Fig. 1e). $\boldsymbol{n_{PV}}$ can be derived by

$$\boldsymbol{n_{PV}} = \boldsymbol{R} \cdot \boldsymbol{n_{PV0}}. \quad (7)$$

Based on above definitions, the following assumptions are made to simplify the physical building structures and the solar radiation models. These assumptions are commonly found in similar studies [46, 49], and are not restrictive as compared with the real scenario.

1. The window is an equator-facing rectangle perpendicular to the horizontal plane. The dimensions of the window and window treatments are

given, whose thicknesses are ignored to simplify the analyses. Window treatments are mounted interiorly behind the window glass, or within the double-glazing window. The transmittance of the outer glass is high, i.e. the absorption and reflection of sunlight can be ignored. The PV window treatments are just able to cover the whole window area for the sake of daylight control and privacy protection, i.e. the total area of PV material S_{PV} equals to wl (Fig. 1c).

2. The shading elements in the window treatments rotate simultaneously so that they receive identical solar irradiance, which benefits the performance of series-connected mini modules. Therefore, the position of an individual shading element can be obtained from one target shading element by a simple translation.

3. The total diffuse irradiance on the PV surface from the sky, ground, and interior reflection is isotropic. In other words, the surface receives identical diffuse irradiance from any direction. The ground-reflected irradiance $G_{t,ground}$ is ignored here. We also simply take the irradiance on the shading area as the isotropic diffuse irradiance, i.e. $G_{h,d}$.

According to aforementioned definitions and assumptions, we can build an isotropic solar irradiance model for the sun-tracking PV window. Since $\cos\gamma$ equals to $\boldsymbol{n_{PV}}^{\mathrm{T}} \cdot \boldsymbol{n_s}$, where the symbol T indicates the transpose operator, referring Eqs. 2 and 7, the global irradiance on the tilt PV shading element $G_{t,global}$ is derived as

$$G_{t,global} = I_e^{dir} \boldsymbol{n_{PV}}^{\mathrm{T}} \cdot \boldsymbol{n_s} + G_{h,d} = I_e^{dir} (\boldsymbol{R} \cdot \boldsymbol{n_{PV0}})^{\mathrm{T}} \cdot \boldsymbol{n_s} + G_{h,d}. \tag{8}$$

According to Assumption 3, the irradiance on the shading area of the PV surface is $G_{h,d}$. Therefore, the solar input power on a diffuse partially-shaded plane is derived as

$$P_{in} = G_{t,global} S_b + G_{h,d}(S_{PV} - S_b) = I_e^{dir} S_b (\boldsymbol{R} \cdot \boldsymbol{n_{PV0}})^{\mathrm{T}} \cdot \boldsymbol{n_s} + G_{h,d} S_{PV}, \tag{9}$$

where S_{PV} indicates the entire PV area. In this model, the solar position ($\boldsymbol{n_s}$) of a specific date and time is predictable with the given longitude and latitude

[53]; I_e^{dir} and $G_{h,d}$ are accessible climate data [5]; $\boldsymbol{n_{PV0}}$ and S_{PV} are constants; S_b can be treated as a function of $\boldsymbol{R}$ for certain geometrical structures of shading elements. Therefore, an optimum $\boldsymbol{R}$ is the key solution to meet aforementioned objectives.

Notably, we consider that the shading elements are covered with lightweight thin-film PV materials. In industry, thin film PV modules contain series-connected solar cells formed by laser scribing technology, which makes it difficult to integrate bypass diodes. Therefore, PV modules in shadows are possible to suffer from the partial shading effects. Also, we assume the shape of solar cells is rectangular, which is the standard shape for industrial PV cells and modules, though other geometric design is possible [54].

2.2. Models of $G_{t,global}$ and shadows on PV shading elements

According to Eq. 9, the global irradiance on the tilt PV shading element $G_{t,global}$ and shadows on PV shading elements are two key models to derive the input power P_{in}. Furthermore, shadows also affect the module efficiency η_m, then consequently affect the output power P_{out} of the PV module (Eq. 4). Here, $G_{t,global}$ and shadows are studied under three types of sun-tracking conditions.

2.2.1. One-DOF sun tracking

In daily life, a most common window treatment with one DOF is a Venetian blind, which usually contains several identical rectangular slats (Fig. 2a). In terms of the model mentioned above, one DOF here refers to the rotation of the rigid PV plane around a single horizontal axis. Mathematically, we use the rotation matrix $\boldsymbol{R_y}(\theta_y)$ to describe such rotations (Fig. 2b), i.e.,

$$\boldsymbol{R_y}(\theta_y) = \begin{bmatrix} \cos\theta_y & 0 & -\sin\theta_y \\ 0 & 1 & 0 \\ \sin\theta_y & 0 & \cos\theta_y \end{bmatrix}, \tag{10}$$

where the rotation is around y-axis; θ_y equals to α_{PV}. According to Eq. 8, $G_{t,global}$ can be derived as

$$G_{t,global} = I_e^{dir}(x_s \cos\theta_y + z_s \sin\theta_y) + G_{h,d}. \tag{11}$$

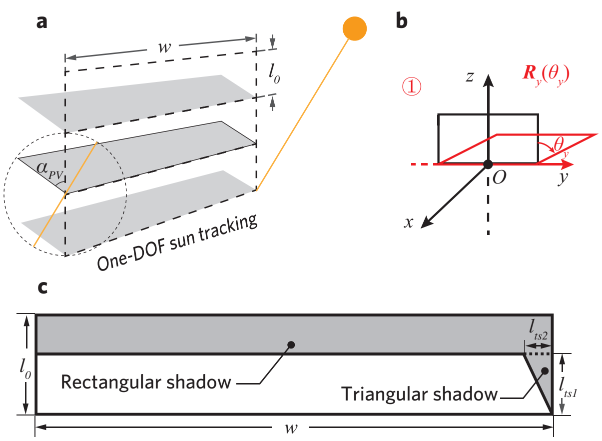

Figure 2: **One-DOF sun tracking with a horizontal axis.**

Typical shadows on the individual slat are observed as shown in Fig 2c. The rectangular shadow comes from the upper slat and only exists in a certain range of θ_y. The triangular shadow is casted by the window frame or wall. Here, shadows are basically determined by two parameters, l_{ts1} and l_{ts2}, as labeled in Fig 2c. Using the basic knowledge of solid analytical geometry, l_{ts1} and l_{ts2} are derived as shown in Eq. 12 and Eq. 13 respectively (see Supplementary Note 3 for detailed derivations).

$$l_{ts1} = \begin{cases} l_0, & \arctan\dfrac{z_s}{x_s} - \dfrac{\pi}{2} \leqslant \theta_y < 0; \\ \dfrac{l_0 x_s}{x_s \cos\theta_y + z_s \sin\theta_y}, & 0 \leqslant \theta_y \leqslant 2\arctan\dfrac{z_s}{x_s}; \\ l_0, & 2\arctan\dfrac{z_s}{x_s} < \theta_y \leqslant \arctan\dfrac{z_s}{x_s} + \dfrac{\pi}{2}. \end{cases} \tag{12}$$

$$l_{ts2} = \left| \frac{l_0 y_s \sin\theta_y}{x_s \cos\theta_y + z_s \sin\theta_y} \right|. \tag{13}$$

The direct-beam-illuminated PV area on the individual slat S_{b0} in this model is then derived as

$$S_{b0} = l_{ts1} w - \frac{1}{2} l_{ts1} l_{ts2}. \tag{14}$$

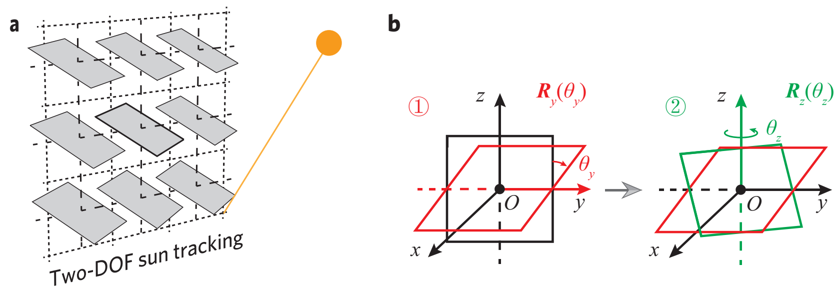

Figure 3: **Two-DOF sun tracking and definition of rotation angles**

2.2.2. *Two-DOF sun tracking*

Dual-axis sun tracking is commonly used in PV power stations since it can maximize P_{in} by positioning PV panels perpendicular to the sunbeam [48]. In this model, two-DOF refers to free rotations of the PV shading element around two axes (Fig. 3a). To achieve free rotations around both axes, we define that shading elements are identical squares; and the centre of each square is its pivot, i.e. the cross point of two axes. According to Assumption 2, we only need to study the rotation of an individual shading element because the positions of other squares can be obtained by simple translations due to fixed pivots. Therefore, we define the centre of the target square as the origin of the Cartesian coordinates. The altitude of the target PV square α_{PV} varies with the rotation around y-axis, denoted by the rotation matrix $\boldsymbol{R_y}(\theta_y)$ (see Eq. 10). The azimuth of the target PV square A_{PV} is changed by the rotation around z-axis, denoted by the rotation matrix $\boldsymbol{R_z}(\theta_z)$, i.e.,

$$\boldsymbol{R_z}(\theta_z) = \begin{bmatrix} \cos\theta_z & -\sin\theta_z & 0 \\ \sin\theta_z & \cos\theta_z & 0 \\ 0 & 0 & 1 \end{bmatrix}. \tag{15}$$

The orientations of θ_y and θ_z are illustrated in Fig. 3b. According to Eq. 8, $G_{t,global}$ can be further derived as

$$\begin{aligned} G_{t,global} &= I_e^{dir}(\boldsymbol{R_z}(\theta_z) \cdot \boldsymbol{R_y}(\theta_y) \cdot \boldsymbol{n_{PV0}})^{\mathrm{T}} \cdot \boldsymbol{n_s} + G_{h,d} \\ &= I_e^{dir}(x_s \cos\theta_y \cos\theta_z + y_s \cos\theta_y \sin\theta_z + z_s \sin\theta_y) + G_{h,d}. \end{aligned} \tag{16}$$

It's interesting to notice that the one-DOF sun tracking can be regarded as a special case of the two-DOF sun tracking. Comparing with the one-DOF case, the PV shading elements with two DOFs produce more complicated patterns of shadows, whose area has no closed-form solution. In order to calculate S_b with arbitrary θ_y and θ_z, a series of algorithms have been developed considering all possible conditions of shading by other squares (see Supplementary Note 5 for detailed algorithms).

2.2.3. Three-DOF sun tracking

Based on two-DOF rotational elements, one more DOF is added to the rotation of the PV shading elements. As before, the centre of the target PV square is defined as its pivot, i.e. the cross point of the three axes. Note that the position of the pivot does change the relative positions of all squares. Thus, the centre can be used as the pivot, when we study the shadows on the target square from its surrounding neighbors. The three-DOF sun tracking can be taken as three-step rotations and mathematically defined using three rotation matrices (Fig. 4). The first and second rotations can be mathematically denoted by the rotation matrices $\boldsymbol{R_y}(\theta_y)$ and $\boldsymbol{R_z}(\theta_z)$, which are exactly the same as those in the two-DOF model. The third rotation is denoted as $\boldsymbol{R_n}(\theta_n)$, which means that the target square rotates θ_n around its normal $\boldsymbol{n_{PV}}$ clockwise (viewing from the positive direction of $\boldsymbol{n_{PV}}$). After the first and second rotations, $\boldsymbol{n_{PV}}$ is derived from the initial PV orientation $\boldsymbol{n_{PV0}}(1, 0, 0)$ as

$$\boldsymbol{n_{PV}} = \begin{bmatrix} x_n \\ y_n \\ z_n \end{bmatrix} = \boldsymbol{R_z}(\theta_z) \cdot \boldsymbol{R_y}(\theta_y) \cdot \boldsymbol{n_{PV0}} = \begin{bmatrix} \cos\theta_y \cos\theta_z \\ \cos\theta_y \sin\theta_z \\ \sin\theta_y \end{bmatrix}. \tag{17}$$

The third rotation matrix $\boldsymbol{R_n}(\theta_n)$ can be expressed as

$$\boldsymbol{R_n}(\theta_n) = \boldsymbol{\hat{n}_{PV}} + \cos\theta_n(\boldsymbol{I} - \boldsymbol{\hat{n}_{PV}}) - \sin\theta_n \boldsymbol{n^*_{PV}}, \tag{18}$$

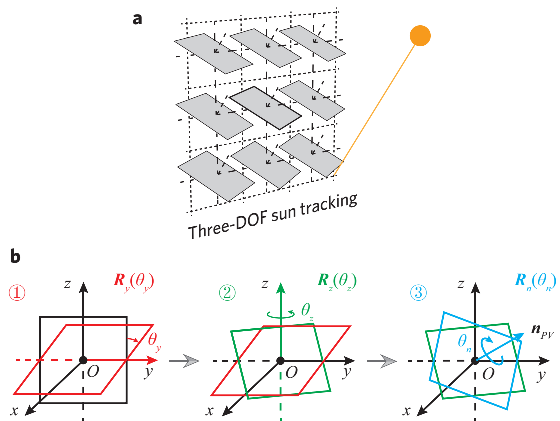

Figure 4: **Three-DOF sun tracking and definition of rotation angles**

where $\hat{\boldsymbol{n}}_{\boldsymbol{PV}}$ and $\boldsymbol{n}^*_{\boldsymbol{PV}}$ can be obtained by Eq. 19 and 20, i.e.

$$\hat{\boldsymbol{n}}_{\boldsymbol{PV}} = \boldsymbol{n}_{\boldsymbol{PV}} \cdot \boldsymbol{n}^{\mathrm{T}}_{\boldsymbol{PV}} = \begin{bmatrix} x_n^2 & x_n y_n & x_n z_n \\ x_n y_n & y_n^2 & y_n z_n \\ x_n z_n & y_n z_n & z_n^2 \end{bmatrix}, \tag{19}$$

$$\boldsymbol{n}^*_{\boldsymbol{PV}} = \begin{bmatrix} 0 & -z_n & y_n \\ z_n & 0 & -x_n \\ -y_n & x_n & 0 \end{bmatrix}, \tag{20}$$

where $\boldsymbol{n}_{\boldsymbol{PV}}(x_n, y_n, z_n)$ is given by Eq. 17.

The overall rotation matrix for the target square with three DOF can be expressed as

$$\boldsymbol{R}_{\boldsymbol{yzn}}(\theta_y, \theta_z, \theta_n) = \boldsymbol{R}_{\boldsymbol{n}}(\theta_n) \cdot \boldsymbol{R}_{\boldsymbol{z}}(\theta_z) \cdot \boldsymbol{R}_{\boldsymbol{y}}(\theta_y). \tag{21}$$

Since the third rotation does not change the normal of the PV square, $G_{t,global}$ in this three-DOF model is the same as that in the two-DOF model (see Eq 16). The aforementioned algorithms are also applicable to the calculation of S_b on the three-DOF PV squares.

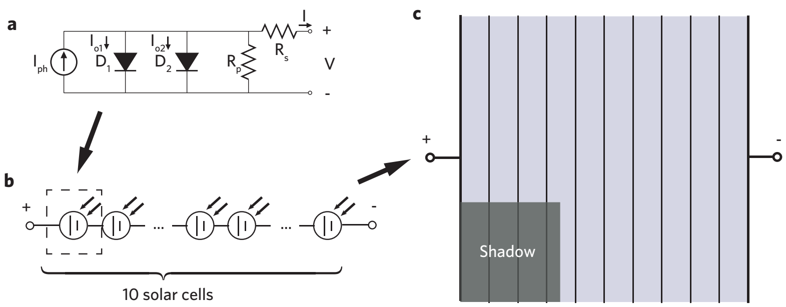

Figure 5: **Model of solar cell and PV module in shadows**

2.3. PV partial-shading model

2.3.1. Model of solar cell and PV module

The two-diode model of the solar cell is used to simulate the PV power generation in certain conditions of irradiance. The equivalent circuit is shown in Fig. 5, where the output current is described as

$$I = I_{ph} - I_{o1}[exp(\frac{V + IR_s}{a_1 V_{T1}}) - 1] - I_{o2}[exp(\frac{V + IR_s}{a_2 V_{T2}}) - 1] - (\frac{V + IR_s}{R_p}), \quad (22)$$

where I_{ph} is the light-induced current. I_{o1} and I_{o2} are the reverse saturation currents of diode 1 and diode 2 respectively. V is the voltage across the solar cell electrical ports. R_s and R_p are the series and parallel resistances respectively. a_1 and a_2 are the quality factors (or called diode emission coefficients) of diode 1 and diode 2 respectively. $V_{T1,2}$ denotes the thermal voltage of the PV module having N_s cells connected in series, defined as,

$$V_{T1,2} = N_s \frac{kT}{q} \quad (23)$$

where k is the Boltzmann constant ($1.3806503 \times 10^{-23}\, J/K$) , T is the temperature of the p-n junction, and q is the electron charge ($1.60217646 \times 10^{-19}\, C$). Detailed model description can be found in [55]. The solar cell model in MATLAB Simulink is simplified by 5 parameters. In this study, the model is parameterized according to the data sheet of a commercially available thin film Silicon PV module (see Supplementary Note 2 for detailed information). Note that the parameters vary according to the dimensions of the target solar cell. Following simulation results are based on those parameters.

2.3.2. Model of equivalent irradiance for partial shading

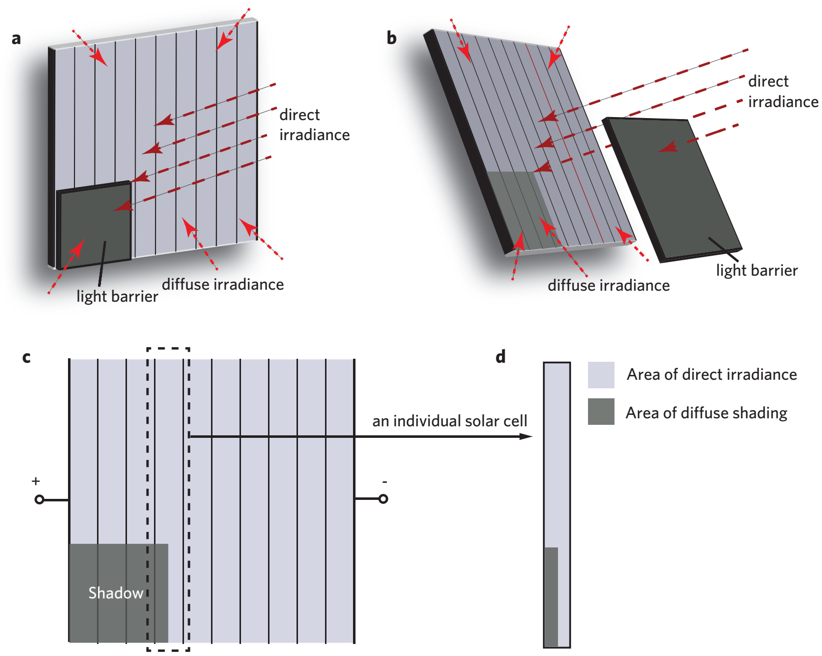

Figure 6: **Partial shading on the PV module**

In reality, two types of shading conditions are commonly observed, complete and diffuse shading conditions. As shown in Fig. 6a, the irradiance of the shading area is zero when it comes to the complete shading condition, e.g. a leaf on the PV panel. As to the diffuse shading condition, the shading area still receives the solar irradiance, e.g. the shadow of a tree on the PV panel. As shown in Fig. 6b, we simply take the horizontal diffuse irradiance $G_{h,d}$ as the solar irradiance on the diffuse shading area.

To simulate the partial shading effects, the equivalent global irradiance $G^{eq}_{t,global}$ of an individual solar cell is derived as

$$G^{eq}_{t,global} = \frac{I_e^{dir} \boldsymbol{n}_{\boldsymbol{PV}}^{\intercal} \cdot \boldsymbol{n}_{\boldsymbol{s}} S_b^i + G_{h,d} S_{PV}^i}{S_{PV}^i} = \frac{S_b^i}{S_{PV}^i} I_e^{dir} \boldsymbol{n}_{\boldsymbol{PV}}^{\intercal} \cdot \boldsymbol{n}_{\boldsymbol{s}} + G_{h,d} \tag{24}$$

where S_b^i is the direct-beam-illuminated area on the individual solar cell. S_{PV}^i is the total area of the individual solar cell. $G_{t,global}^{eq}$ is a critical input of the partial-shading simulation. S_b^i can be derived by the aforementioned models of shadows under different sun-tracking methods.

2.4. Glare model

To evaluate the visual comfort under different sun-tracking methods, the Rhinoceros model of a reference room is used in this study [52]. In this model, point-in-time glare can be calculated by Grasshopper, a graphical algorithm editor tightly integrated with Rhinoceros.

Currently, there is a number of different indices for assessing visual comfort [56]. In this study, we use Unified Glare Rating (UGR) and Discomfort Glare Probability (DGP) to evaluate the level of glare.

2.4.1. Unified Glare Rating (UGR)

CIE's Unified Glare Rating (UGR) is defined as

$$UGR = 8log_{10}[\frac{0.25}{L_b}\sum_{i=1}^{N}(\frac{L_{s,t}^2\omega_{s,t}}{P_i^2})]. \tag{25}$$

$$\text{subject to } \omega_s \in [3\times 10^{-4}, 10^{-1}]sr$$

where the subscript s is used for those quantities depending on the observer position and i for those quantities depending on the light sources. L_b is the background luminance. $L_{s,t}$ is the luminance in the direction connecting the observer with each source. $\omega_{s,t}$ is the solid angle subtending the source i from the position of the observer. P is the Guth position index, expressing the dependence of perceived discomfort glare on the position of the source i with respect to the observer. UGR ranges between 10 (imperceptible) to 34 (intolerable) with a three-unit step [56].

2.4.2. Discomfort Glare Probability (DGP)

Discomfort Glare Probability (DGP) is is defined as

$$DGP = 5.87\times 10^{-5}E_v + 0.0918log_{10}[1+\sum_{i=1}^{N}(\frac{L_{s,t}^2\omega_{s,t}}{E_v^{1.87}P_i^2})] + 0.16, \tag{26}$$

where E_v is the vertical eye illuminance. DGP reveals a stronge correlation with the user′s response regarding glare perception [56].

3. Results

To give the optimum sun-tracking solutions, a typical set of climate data of Shanghai (see Supplementary Note 4) is used for the calculation and simulation of $G_{t,global}$, S_b, P_{in}, and point-in-time glare under all possible sun-tracking positions. Then, accumulated power generation (E_a) and average efficiency ($\bar{\eta}_m$) over the year under conventional and the proposed optimum sun-tracking methods are simulated and compared. Lastly, results of nine global cities are obtained to conclude a general improvement of E_a and $\bar{\eta}_m$ by using the proposed method.

3.1. Optimum sun-tracking solutions

3.1.1. One-DOF sun tracking

As discussed in the model of one-DOF PV blind, rectangular and triangular shadows are observed in the typical shading conditions. Usually, the area of triangular shadow on a long narrow slat is negligible due to its relatively small size. Therefore, Eq. 14 is simplified as

$$S_{b0} = l_{ts1} w. \tag{27}$$

In this case, according to Eq. 9, the input power P_{in} for all slats in the PV blind is derived as

$$P_{in} = \begin{cases} I_e^{dir} lw(x_s \cos\theta_y + z_s \sin\theta_y) + G_{h,d} lw, & \arctan\dfrac{z_s}{x_s} - \dfrac{\pi}{2} \leqslant \theta_y < 0; \\ I_e^{dir} lw x_s + G_{h,d} lw, & 0 \leqslant \theta_y \leqslant 2\arctan\dfrac{z_s}{x_s}; \\ I_e^{dir} lw(x_s \cos\theta_y + z_s \sin\theta_y) + G_{h,d} lw, & 2\arctan\dfrac{z_s}{x_s} < \theta_y \leqslant \arctan\dfrac{z_s}{x_s} + \dfrac{\pi}{2}. \end{cases} \tag{28}$$

We notice that P_{in} is independent of l_0, the length of the individual slat. It means that the number of slats does not affect P_{in} as long as the dimension of the window is given and the triangular shadows are ignored. We also notice that P_{in} remains maximum when $\theta_y \in [0, 2\arctan(z_s/x_s)]$, which means the quasi-perpendicular position ($\theta_y = \arctan(z_s/x_s)$) where $G_{t,global}$ reaches the peak is not the only option for the maximum P_{in} (see Supplementary Note 3 for detailed explanations). To better illustrate $G_{t,global}$, S_b, and P_{in} in different tilt positions, a set of example data is introduced (see Supplementary Note 4) to draw the semicircular color maps (Fig. 7b, c, d).

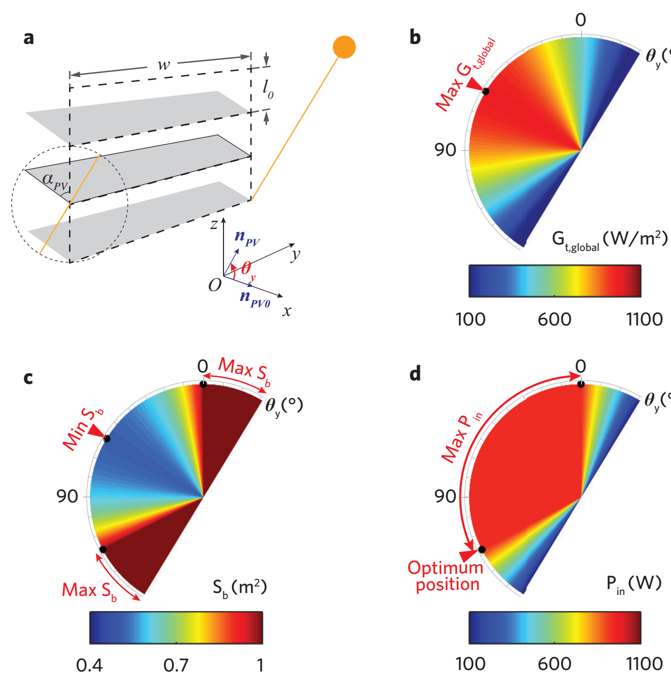

Figure 7: **Simulation results of all possible one-DOF sun tracking positions**

Referring to Eq. 4, the maximum P_{out} is gained with the maximum P_{in} and η_m, i.e. no shadow on the PV plane ($S_b = S_{PV}$). In regard to this one-DOF PV blind, the optimum position is located where θ_y equals to 0 or $2\arctan(z_s/x_s)$. However, $\theta_y = 0$ means the blind stays in the closed position forever, which is not appropriate, because it turns the window into a PV wall and disables the function of daylighting. Therefore, the only feasible option of the optimum θ_y is $2\arctan(z_s/x_s)$.

Shadow simulation in a SketchUp [51] model (Fig. 8) demonstrates that

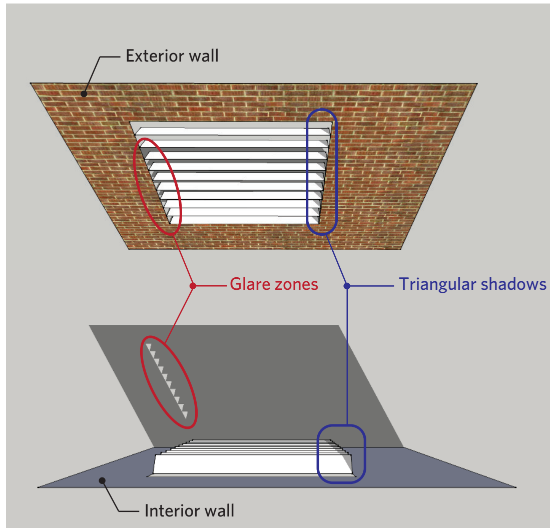

Figure 8: **Shadow simulation of the optimum position of one-DOF shading elements by SketchUp [51]. Interior glare zones (red) and triangular shadows (blue) on the slats are marked.**

this optimum θ_y can effectively avoid rectangular shadows from upper slats. However, it cannot eliminate triangular shadows from window frames. Such triangular shadows are ignored when we estimate P_{in} because of the small area. But they cannot be ignored regarding η_m due to partial shading effects of PV modules. What is worse, on the other side of the blind, incident sunlight forms glare zones in the interior space. We have also tested the PV blind with vertical slats, whose optimum position ($\theta_z = 2(\pi - A_s)$) cannot avoid triangular shadows and glare zones either (see Supplementary Note 3). Therefore, we conclude that PV window treatments with one DOF are not able to achieve the maximum P_{out} and not able to avoid glare in the optimum position in the proposed model. Despite the restrictions of this model, improved design of the one-DOF PV blind will be discussed later.

3.1.2. Two-DOF sun tracking

As mentioned above, algorithms are developed for the calculation of two-DOF sun tracking method. By using the same data set, $G_{t,global}$, S_b and P_{in}

are calculated under a full range of conditions of θ_y and θ_z (see Supplementary Note 5). As before, we ignore the shadows from walls and window frames at first.

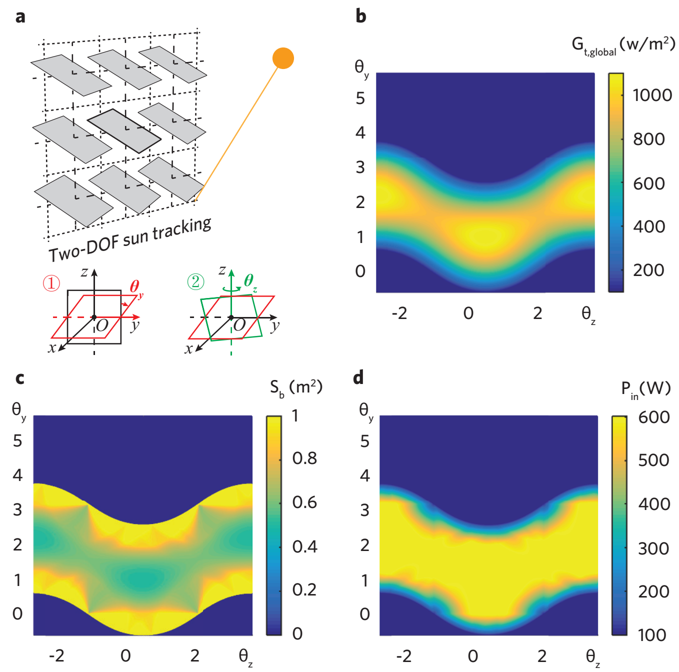

Figure 9: **Simulation results of all possible two-DOF sun tracking positions.**

Apparently, $G_{t,global}$ hits the peak when the PV plane is perpendicular to the sunbeam (Fig. 9b). However, S_b reaches the its minimum value at the very same position (Fig. 9c). As their product, P_{in} remains the maximum within a certain range, instead of a single point (Fig. 9d). This conclusion is similar to that under the one-DOF conditions (Fig. 7d). To have the maximum P_{out}, the optimum position should be located where P_{in} and S_b climb to the peak simultaneously.

To illustrate this issue clearly, two-dimensional maps of the three parameters are drawn together as show in Fig. 10. If the optimum position exists, theoretically, there are infinitely many such positions since periodic patterns

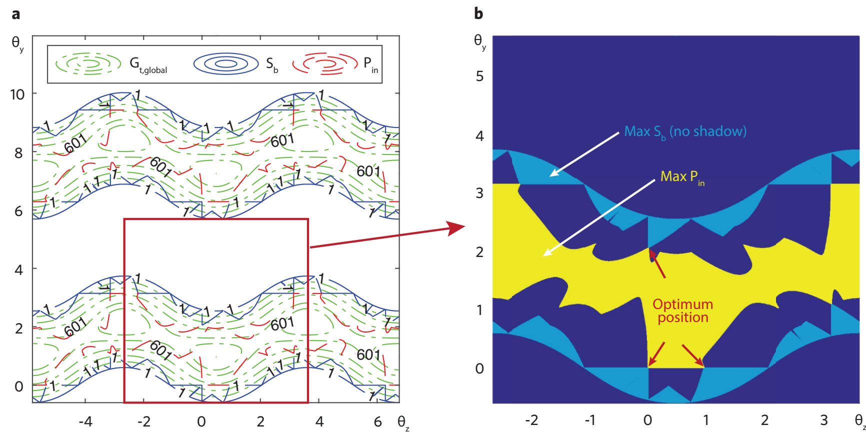

Figure 10: **Two-dimensional maps of $G_{t,global}$, S_b, and P_{in}**

are observed for $G_{t,global}$, S_b, and P_{in} (Fig. 10a). Therefore, we only focus on the period nearest to the initial position, where three eligible positions are found (Fig. 10b). However, such three positions are located at either $\theta_y = 0$ or $\theta_z = 0$, i.e., they are equivalent to the one-DOF sun tracking. Specifically, among the three optimum positions in the θ_z-θ_y coordinates (Fig. 10b), $(0, 0)$ indicates the closed position, which is meaningless for windows as discussed before; $(0, 2\arctan(z_s/x_s))$ and $(2(\pi - A_s), 0)$ represent the optimum positions of the one-DOF sun tracking with horizontal axes and vertical axes respectively. Therefore, in terms of the optimum position of sun tracking, the PV shading elements with two DOFs perform exactly the same as that with one DOF. Triangular shadows caused by walls and window frames affect the module efficiency the same way as discussed in one-DOF sun tracking. Therefore, we can draw a similar conclusion that PV window treatments with two DOFs are not able to achieve the maximum P_{out} and not able to avoid glare in the optimum position in the proposed model.

3.1.3. Three-DOF sun tracking

Comparing with the two-DOF rotations, the three-DOF sun tracking requires one more dimension to illustrate the results of $G_{t,global}$, S_b, and P_{in} as

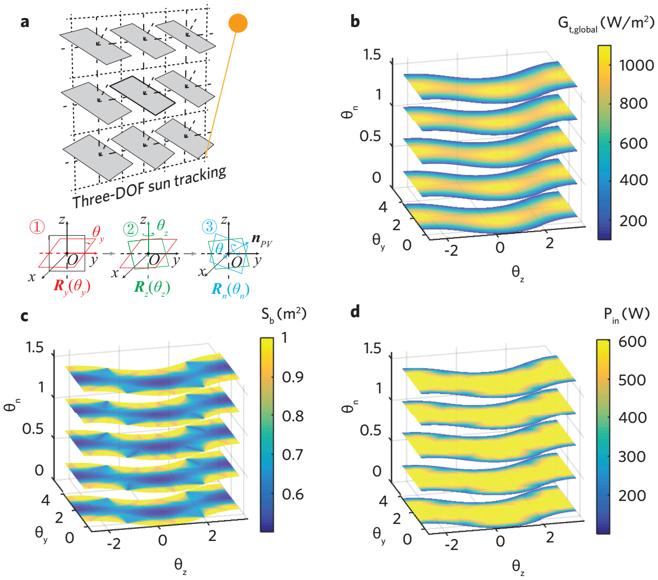

Figure 11: **Simulation results of all possible three-DOF sun tracking positions.**

shown in Fig. 11. Therefore, it is difficult to determine the optimum positions by only visual observation. According to Eq. 21, an optimum $\boldsymbol{R_{yzn}}(\theta_y, \theta_z, \theta_n)$ corresponds to an optimum sun-tracking position, where the maximum P_{in} and η_m are observed. Therefore, theoretically, the optimum $\boldsymbol{R_{yzn}}(\theta_y, \theta_z, \theta_n)$ can be derived based on the following two main conditions. First, there shall be no shadow on the target square from surrounding squares. Second, the input power P_{in} shall stay the maximum, which is the same as that in the initial position.

To derive the optimum $\boldsymbol{R_{yzn}}(\theta_y, \theta_z, \theta_n)$, the critical intermediate equations are obtained based on the principles of solid analytic geometry (see Supplementary Note 6 for details). The key closed-form relations between the rotation angles and the solar position are presented in Eq. 29.

$$\begin{cases} \cos\theta_y \cos\theta_z = 2x_s^2 - 1, \\ \cos\theta_y \sin\theta_z = 2x_s y_s, \\ \sin\theta_y = 2x_s z_s, \\ \cos\theta_n = 2x_s y_s \sin\theta_z + (1 - 2y_s^2)\cos\theta_z, \\ \sin\theta_n = \dfrac{z_s}{x_s}\sin\theta_z. \end{cases} \tag{29}$$

First, it is easy to derive θ_y, i.e.

$$\theta_y = (-1)^{(k_y)} \arcsin(2x_s z_s) + k_y\pi,\ k_y \in \mathbb{Z}, \tag{30}$$

where k_y is an arbitrary integer. By substituting θ_y into Eq. 29, θ_z is derived as

$$\theta_z = \pm\arccos\left(\frac{2x_s^2 - 1}{\cos\theta_y}\right) + 2k_z\pi,\ k_z \in \mathbb{Z}, \tag{31}$$

where k_z is an arbitrary integer. From Eq. 29, we can also derive θ_n, i.e.

$$\theta_n = \begin{cases} -\arccos[2x_s y_s \sin\theta_z + (1 - 2y_s^2)\cos\theta_z], & \dfrac{z_s \sin\theta_z}{x_s} < 0; \\ \arccos[2x_s y_s \sin\theta_z + (1 - 2y_s^2)\cos\theta_z], & \dfrac{z_s \sin\theta_z}{x_s} \geqslant 0, \end{cases} \tag{32}$$

where $\theta_n \in [-\pi, \pi]$, which includes a complete cycle.

To verify the above derivations and determine k_y and k_z, the same example data and algorithms are applied to calculate S_b and P_{in} as discussed previously. Apparently, θ_n does not affect $G_{t,global}$ at all because it does not change α_{PV} and A_{PV} (Fig. 11b). However, it changes the shadows on the squares, and thus influences S_b (Fig. 11c). Therefore, P_{in} varies with θ_n, θ_z, and θ_y (Fig. 11d). From the periodical contours of $G_{t,global}$, S_b, and P_{in}, we can conclude that the solutions can fulfill the optimum conditions. The optimum position nearest to the initial position is found, where $k_y = 1$ and $k_z = 0$ (Fig. 12a). Therefore, the

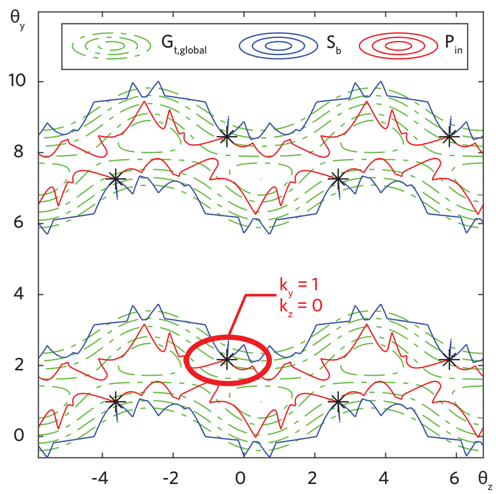

Figure 12: **A periodic contour map of $G_{t,global}$ (green), S_b (blue), and P_{in} (red) on the squares as a function of θ_y, θ_z, and θ_n, where the value of θ_n is obtained by Eq. 32. The solution points are marked with stars, among which the one in the red circle is nearest to the initial position.**

optimum rotation angles for the three-DOF sun tracking are concluded as

$$\begin{cases} \theta_y = \pi - \ arcsin(2x_s z_s), \\ \theta_z = \begin{cases} -\arccos(\dfrac{2x_s^2 - 1}{\cos\theta_y}), & x_s y_s \cos\theta_y < 0; \\ \arccos(\dfrac{2x_s^2 - 1}{\cos\theta_y}), & x_s y_s \cos\theta_y \geqslant 0, \end{cases} \\ \theta_n = \begin{cases} -\arccos[2x_s y_s \sin\theta_z + (1 - 2y_s^2)\cos\theta_z], & \dfrac{z_s \sin\theta_z}{x_s} < 0; \\ \arccos[2x_s y_s \sin\theta_z + (1 - 2y_s^2)\cos\theta_z], & \dfrac{z_s \sin\theta_z}{x_s} \geqslant 0. \end{cases} \end{cases} \tag{33}$$

Besides the solutions mentioned above, we also found other solutions meeting the optimum conditions. However, those solutions share a common problem that they cannot avoid the shadows from walls and window frames, even without the shadows coming from the surrounding squares (see Supplementary Note 6). Only the solution provided by Eq. 33 describes the shadows with the same shape as that of the illuminated area through an unshaded window. Therefore, this solution is the only one capable of avoiding shadows from walls and window

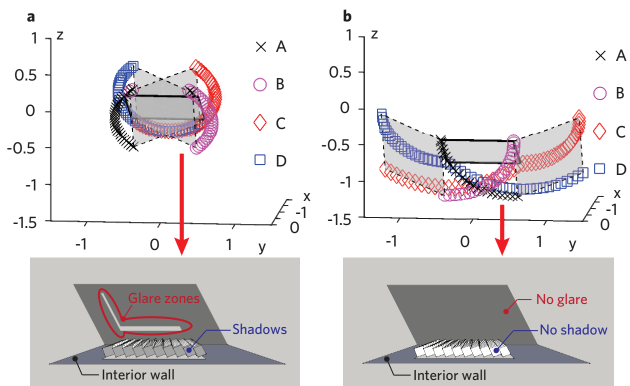

Figure 13: **Optimum solutions to three-DOF sun tracking a,** A schematic of the trajectories of a PV square with the optimum three-DOF sun tracking and the corresponding SketchUp simulation, where shadows are found on PV squares; and glare zones are found interior. The pivot is fixed in the centre of the PV square. **b,** A schematic of the trajectories of a PV square with the optimum variable-pivot-three-DOF sun tracking and the corresponding SketchUp simulation, where neither shadow nor glare is found. The pivot is variable from the corner A to B according to θ_z. Visualizations of 3-DOF and VP-3-DOF rotations are provided in Supplementary Video 1.

frames.

However, this solution for the three-DOF sun tracking still suffers from shading, when the pivots lie in the centre of the PV squares. Though the shape of shadows fulfills the requirement, the deviation of shadows caused by the fixed centres leads to interior glares and shadows on the PV squares from walls and window frames (Fig. 12b). Fortunately, a trick is found to eliminate such a deviation by changing the position of the pivot according to the solar position. Specifically, the bottom left corner A of the target square is used as the pivot, when the solar azimuth A_s is less than the azimuth of the window. Similarly, the right bottom corner B is taken as the pivot, when A_s is greater than the azimuth of the window (Fig. 12c). Mathematically, to switch the pivot from the centre to the corner A or B, translations are required before and after the rotations. Let $Q_0(x_{q0}, y_{q0}, z_{q0})$ be an arbitrary point on the target square in the initial position, and $Q(x_q, y_q, z_q)$ be the same point after the rotations. Also, we define two translations as $\begin{bmatrix}0 & -l_0/2 & -l_0/2\end{bmatrix}^{\mathrm{T}}$ and $\begin{bmatrix}0 & l_0/2 & -l_0/2\end{bmatrix}^{\mathrm{T}}$, which are the translations from O to A, and from O to B, respectively. Then, the position of Q after the mixed rotations and translations is obtained by

$$\begin{bmatrix}x_q \\ y_q \\ z_q\end{bmatrix} = \begin{cases} \boldsymbol{R_{yzn}}(\theta_y, \theta_z, \theta_n) \cdot \left(\begin{bmatrix}x_{q0} \\ y_{q0} \\ z_{q0}\end{bmatrix} - \begin{bmatrix}0 \\ -l_0/2 \\ -l_0/2\end{bmatrix} \right) + \begin{bmatrix}0 \\ -l_0/2 \\ -l_0/2\end{bmatrix}, & \theta_z \geqslant 0; \\ \boldsymbol{R_{yzn}}(\theta_y, \theta_z, \theta_n) \cdot \left(\begin{bmatrix}x_{q0} \\ y_{q0} \\ z_{q0}\end{bmatrix} - \begin{bmatrix}0 \\ l_0/2 \\ -l_0/2\end{bmatrix} \right) + \begin{bmatrix}0 \\ l_0/2 \\ -l_0/2\end{bmatrix}, & \theta_z < 0. \end{cases} \tag{34}$$

With Eq. 34, we can obtain the trajectories of the four corners of the target square. Such defined mixed rotations and translations can ensure that no shadow is on the PV squares and no glare appears inside (Fig. 12c). The perfect solution comes into effect with three-step rotations (see Eq. 33) and an ingenious switch of pivots (see Eq. 34). Therefore, we name this sun-tracking method as the variable-pivot-three-DOF (VP-3-DOF) sun tracking. Here we use the phrase "3-DOF" instead of "3-axis" because it is not necessary to actually have three axes in the physical structures as long as the corners of the target square move along the trajectories. Note that the pivots only need to switch one time a day when $\theta_z = 0$. The movement of the squares is continuous, as illustrated by the trajectories in Fig. 12c. Therefore, we conclude that the VP-3-DOF sun tracking is able to achieve the maximum power generation and non-glare daylighting for this model.

3.2. Output power generation

3.2.1. Partial shading effects

Based on the aforementioned partial shading model and example data set, the output power of the mini PV module is simulated under various conditions of shadows. As shown in Fig. 14, the results show that the PV module performs the best when no shadow casts upon it. Besides, η_m drops dramatically when uneven shadows are found on series-connected solar cells. The performance of PV power generation is less affected by diffuse shadows than that by complete shadows with the same dimensions.

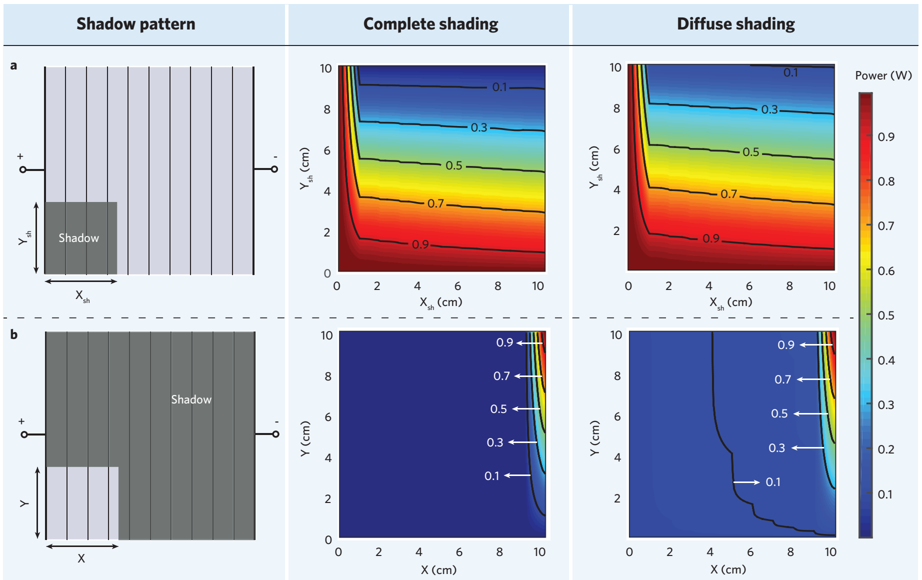

Figure 14: **Simulation results of PV partial shading effects.**

3.2.2. Annual power generation per unit area

Above we succeeded in maximizing the power generation at a certain instant with the VP-3-DOF sun tracking. Now we intend to verify that the VP-3-DOF sun tracking also benefits the annual energy generation and average module efficiency comparing with other sun-tracking methods through simulation studies. Here we mainly consider four sun-tracking methods, i.e. one-DOF quasi-perpendicular, one-DOF optimum, two-DOF perpendicular, and optimum VP-3-DOF sun-tracking methods. Since the performance of the partially-shaded PV modules varies with the pattern of cell layouts, here we consider both layouts of vertical stripes and horizontal stripes.

By inputing a set of $G^{eq}_{t,global}$ for each solar cell in the PV module, the simulation models generate hourly output power and module efficiency. Then the

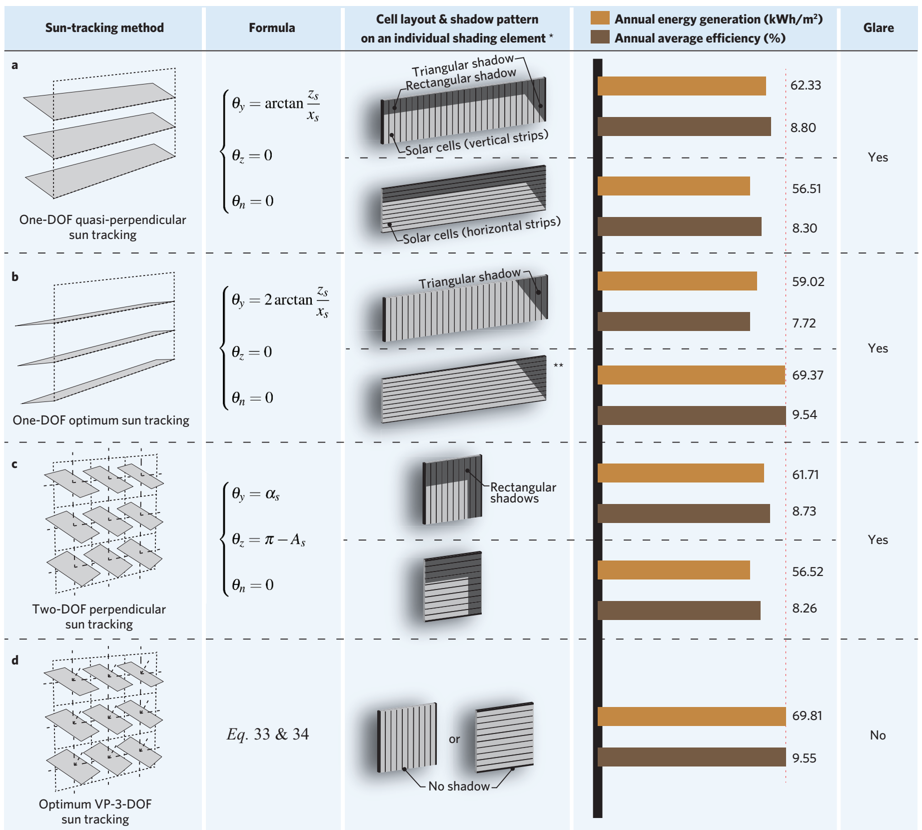

* Note that the number of solar cells on the individual shading element for illustation is not necessarily the same as the that for simulation.

** The performance of the one-DOF optimum sun tracking with slats covered by horizontal solar cells is depending on the ratio of the width (w) to the side length (l_0) of the slat (see Fig. 7).

Figure 15: **Simulation results of four sun-tracking methods and two cell layouts using irradiation data of Shanghai. a,** One-DOF quasi-perpendicular sun tracking. **b,** One-DOF optimum sun tracking. **c,** Two-DOF perpendicular sun tracking. **d,** Optimum variable-pivot-three-DOF sun tracking. Note that in **c** we ignore the shadows from walls and window frames for simplified calculation. Therefore, the actual values of E_a and $\bar{\eta}_m$ in **c** shall be even less than that presented here. The sketch of sun-tracking method in **d** only presents the three-DOF rotations, instead of the variable pivot.

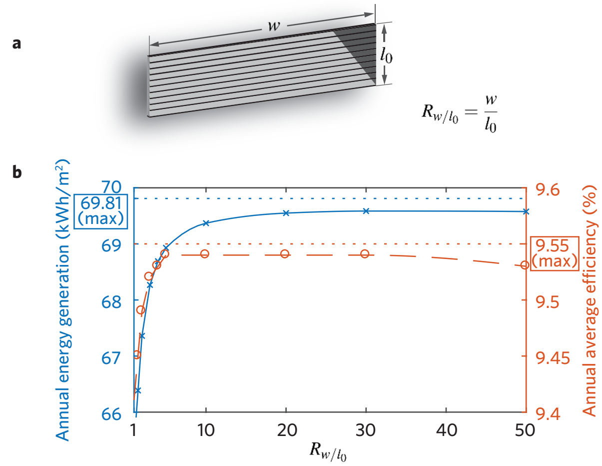

Figure 16: **Definition and influence of** R_{w/l_0}

annual energy generation per unit area (E_a) and the annual average efficiency ($\bar{\eta}_m$) of the PV module can be calculated. The simulation results of four sun-tracking methods are obtained by using the climate data of Shanghai, as shown in Fig. 15. It is obvious that the proposed optimum VP-3-DOF sun-tracking method performs better than others in all the aspects of annual energy generation, annual average efficiency, and glare protection. Though one-DOF optimum sun tracking with horizontal stripes shows competitive results in aspect of E_a and $\bar{\eta}_m$, it cannot protect glare from the sun properly. Besides, the PV performance of one-DOF optimum sun tracking with horizontal stripes depends on the ratio of the width (w) to the side length (l_0) of the slat, i.e. R_{w/l_0} (Fig. 16). E_a and $\bar{\eta}_m$ drop dramatically with the decrease of R_{w/l_0}, and they cannot reach the max value obtained by the optimum VP-3-DOF sun tracking. Therefore, we conclude that the optimum VP-3-DOF sun tracking is capable to gain the maximum annual energy generation and annual average efficiency, and also capable to protect glare from the sun.

Comparing with conventional two-DOF perpendicular sun-tracking method, the proposed optimum VP-3-DOF sun tracking reveal better performance in terms of PV outputs and glare protection. In the example of Shanghai, with the VP-3-DOF sun tracking, E_a is improved by 13.12%; and $\bar{\eta}_m$ is improved by 9.39%. To draw a general conclusion, E_a and $\bar{\eta}_m$ are calculated using the simulation results of the other eight cities in the world. As the average over the nine cities, E_a is improved by 27.40%; $\bar{\eta}_m$ is improved by 19.17% using our proposed optimum VP-3-DOF sun tracking (see Supplementary Note 7).

3.3. Point-time glare

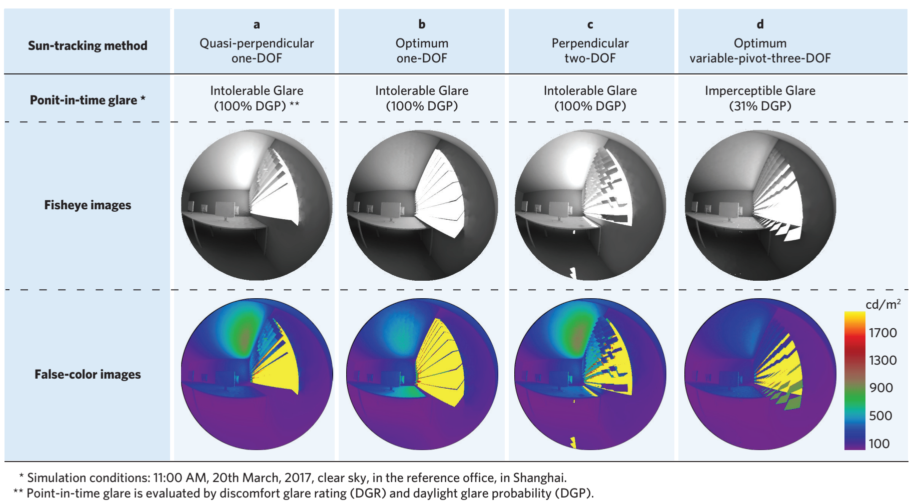

Figure 17: **Simulation results of point-in-time glare by four sun-tracking methods.**

Fig. 17 quantitively and visually shows the simulation results based on the glare model mentioned above. The results of point-in-time glare coincide with the shadow simulations by SketchUp. Particularly, the proposed optimum VP-3-DOF sun tracking reveals imperceptible glare and 31% DGP.

4. Discussion

4.1. Optimum design of one-DOF PV blind

When inevitable shadows are casted on the PV modules, the layout of solar cells determines how serious the PV module suffers from the partial shading

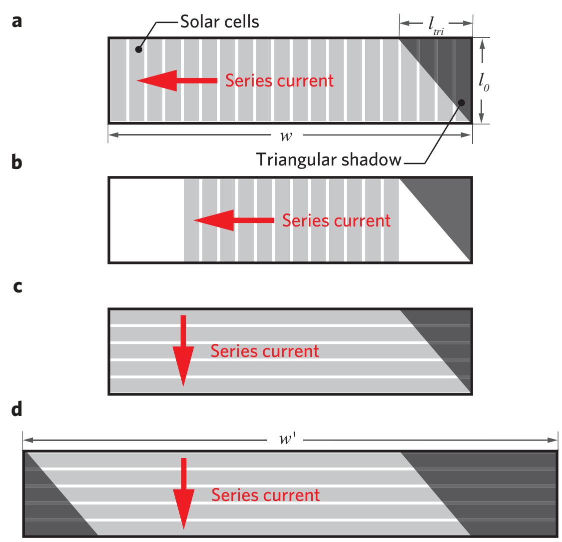

Figure 18: **Optimization of cell layouts for one-DOF sun tracking.**

effects. In terms of the one-DOF sun tracking, triangular shadows caused by walls and window frames are inevitable. In this case, the cell layouts of vertical stripes (Fig 18a) and horizontal stripes (Fig 18c) are affected by partial shading effects. Obviously, vertical stripes suffers more since the series current is limited by the most shaded cell. To alleviate the decrease of PV module efficiency, optimal layouts are applicable if the restriction in Assumption 1 (PV area equals to wl) is relaxed. In regards to vertical stripes, we can leave the shading area blank, i.e. without covering the solar cells (Fig 18b). The length of blank area is $2l_{tri}$, where the side length of the triangular shadow l_{tri} is derived as

$$l_{tri} = \left| \frac{y_s}{x_s} \sin\theta_y \right| l_0. \tag{35}$$

To avoid shadows, l_{tri} shall use the maximum among all possible values. As to horizontal stripes, we can extend the width of the slats to w' (Fig 18d), where

$$w' = w + 2l_{tri}. \tag{36}$$

Theoretically, the improved layout of horizontal stripes is able to achieve the maximum power generation and non-glare daylighting with one-DOF sun tracking ($\theta_y = 2\arctan(z_s/x_s)$). Comparing with the optimum VP-3-DOF sun tracking, the optimum one-DOF sun tracking with the improved layout of horizontal stripes achieve the same performance with simpler mechanical structures. However, the extension of slats costs more PV material, whose area is $2l_{tri}l$ for the window. In contrast, the optimum VP-3-DOF sun tracking does not rely on improved cell layout and costs less PV material to achieve the same goal.

4.2. VP-3-DOF sun tracking

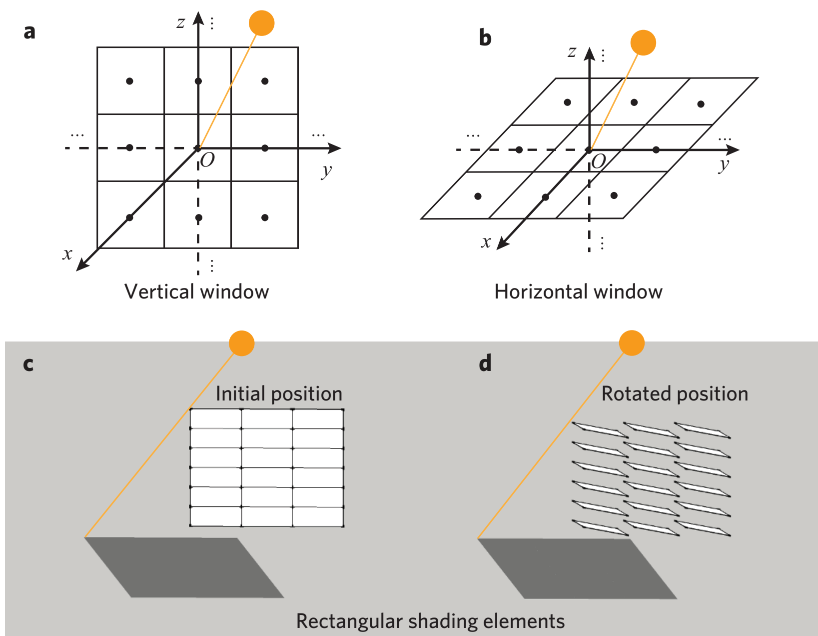

Figure 19: **Extended application of VP-3-DOF sun tracking.**

The mechanical realization of the VP-3-DOF motion is out of the scope of the current study. Some recommendations to realize the VP-3-DOF motion are given as follows. Firstly, it is not necessary to have physical axes to achieve the rotation. The only requirement is to follow the trajectories provided by our mathematical model. Secondly, since it is an interior lightweight application, the use of fine translucent wires can be considered to actuate PV shading elements, similar to but more sophisticated than what the normal window blinds are using.

Thirdly, electrical cables can be considered to be installed along the wires to interconnect the PV modules.

Besides vertical windows, the proposed VP-3-DOF sun tracking is also applicable to the horizontal sun roof. In terms of special scenarios, e.g. a glass greenhouse, the roof area is large and the incident sunlight need to be controlled. Comparing with the case with vertical windows (Fig. 19a), the optimum solution to the case with horizontal windows (Fig. 19b) can be derived in a similar way. Detailed derivations and results are presented in the Supplementary Note 8. A promising applications of the VP-3-DOF sun tracking is in a greenhouse with movable PV roof to utilize the sunlight for both food cultivation and electricity generation (see Supplementary Note 8).

Besides square PV shading elements, the rectangular PV shading elements can also apply to the VP-3-DOF sun tracking. It has been demonstrated by shadow simulations with SketchUp (Fig. 19c & d).

5. Conclusions

In this paper, we have investigated the performance of the one-degree-of-freedom (one-DOF), two-DOF, and three-DOF sun tracking using our proposed irradiance model. Two solutions, the optimum one-DOF sun tracking with the improved layout of horizontal stripes and optimum VP-3-DOF sun tracking, enable the sun-tracking PV window to achieve the maximum power generation and non-glare daylighting at the same time. Comparing with conventional perpendicular sun tracking, the proposed sun tracking methods improve the annual energy generation by 27.40% and the annual average efficiency by 19.17% as the average over nine cities in the world. Such module-level improvements are more pronounced than that triggered by new materials and process in most studies. Comparing the two proposed solutions, the optimum one-DOF sun tracking with extended PV slats and particular cell layout requires simpler mechanical structure of rotations; while the optimum VP-3-DOF sun tracking requires less area of PV material and simpler design of cell layout.

Besides the benefits in energy generation, both solutions provide the building occupants with comfortable diffuse daylight and open exterior view. As an extended application, the optimum VP-3-DOF sun tracking for PV shading elements on horizontal glass roof of a greenhouse is capable to maximize the power generation, and also provides the crops with certain amount of diffuse daylight. An economic PV horticultural system can be built by applying the proposed sun-tracking method, which can increase the production of crops and reduce the energy consumption. Theoretically, the optimum variable-pivot-three-DOF sun-tracking method is applicable to any occasions requiring the maximum power generation and the access to the natural diffuse light.

References

[1] G. Quesada, D. Rousse, Y. Dutil, M. Badache, S. Hallé, A comprehensive review of solar facades. Transparent and translucent solar facades, Renewable and Sustainable Energy Reviews (5) 2643–2651. doi:10.1016/j.rser.2012.02.059.

[2] W. Zhang, L. Lu, J. Peng, A. Song, Comparison of the overall energy performance of semi-transparent photovoltaic windows and common energy-efficient windows in Hong Kong, Energy and Buildings 511–518doi:10.1016/j.enbuild.2016.07.016.

[3] F. Guo, S. Chen, Z. Chen, H. Luo, Y. Gao, T. Przybilla, E. Spiecker, A. Osvet, K. Forberich, C. J. Brabec, Printed Smart Photovoltaic Window Integrated with an Energy-Saving Thermochromic Layer, Advanced Optical Materials 3 (11) (2015) 1524–1529. doi:10.1002/adom.201500314.

[4] N. Skandalos, D. Karamanis, PV glazing technologies, Renewable and Sustainable Energy Reviews 306–322doi:10.1016/j.rser.2015.04.145.

[5] J. Remund, S. Kunz, METEONORM: Global meteorological database for solar energy and applied climatology, Meteotest, 1997.

[6] S.-Y. Lien, C.-H. Hsu, Y.-C. Ou, Innovation and fabrication of 5.5 generation image-patterned translucent photovoltaic module by using laser scribing technology, Progress in Photovoltaics: Research and Applications (3) 374–378. doi:10.1002/pip.1211.

[7] N. Sellami, T. K. Mallick, Optical characterisation and optimisation of a static Window Integrated Concentrating Photovoltaic system, Solar Energy 273–282doi:10.1016/j.solener.2013.02.012.

[8] M. Cossu, A. Yano, Z. Li, M. Onoe, H. Nakamura, T. Matsumoto, J. Nakata, Advances on the semi-transparent modules based on micro solar cells: First integration in a greenhouse system, Applied Energy 1042–1051doi:10.1016/j.apenergy.2015.11.002.

[9] K. Kapsis, A. Athienitis, Building integrated semi-transparent photovoltaics: energy and daylighting performance, in: R. Kashyap, M. Têtu, R. N. Kleiman (Eds.), Photonics North 2011, International Society for Optics and Photonics, pp. 800726–800726–11. doi:10.1117/12.911450.

[10] K. Kapsis, V. Dermardiros, A. K. Athienitis, Daylight Performance of Perimeter Office Façades utilizing Semi-transparent Photovoltaic Windows: A Simulation Study, Energy Procedia 334–339doi:http://dx.doi.org/10.1016/j.egypro.2015.11.657.

[11] A. Yano, M. Onoe, J. Nakata, Prototype semi-transparent photovoltaic modules for greenhouse roof applications, Biosystems Engineering 62–73doi:10.1016/j.biosystemseng.2014.04.003.

[12] A. Takeoka, S. Kouzuma, H. Tanaka, H. Inoue, K. Murata, M. Morizane, N. Nakamura, H. Nishiwaki, M. Ohnishi, S. Nakano, Y. Kuwano, Development and application of see-through a-Si solar cells, Solar Energy Materials and Solar Cells (3) 243–252. doi:10.1016/0927-0248(93)90039-6.

[13] S. Yeop Myong, S. Won Jeon, Design of esthetic color for thin-film silicon

semi-transparent photovoltaic modules, Solar Energy Materials and Solar Cells 442–449doi:10.1016/j.solmat.2015.07.042.

[14] J. Han, L. Lu, H. Yang, Numerical evaluation of the mixed convective heat transfer in a double-pane window integrated with see-through a-Si PV cells with low-e coatings, Applied Energy (11) 3431–3437. doi:10.1016/j.apenergy.2010.05.025.

[15] S. H. Moon, S. J. Park, Y. J. Hwang, D.-K. Lee, Y. Cho, D.-W. Kim, B. K. Min, Printable, wide band-gap chalcopyrite thin films for power generating window applications., Scientific reports 4408doi:10.1038/srep04408.

[16] Y. Yang, P. G. O'Brien, G. A. Ozin, N. P. Kherani, See-through amorphous silicon solar cells with selectively transparent and conducting photonic crystal back reflectors for building integrated photovoltaics, Applied Physics Letters (22) 221109. doi:10.1063/1.4833542.

[17] J. Han, L. Lu, H. Yang, Numerical evaluation of the mixed convective heat transfer in a double-pane window integrated with see-through a-Si PV cells with low-e coatings, Applied Energy (11) 3431–3437. doi:10.1016/j.apenergy.2010.05.025.

[18] J. Peng, D. C. Curcija, L. Lu, S. E. Selkowitz, H. Yang, W. Zhang, Numerical investigation of the energy saving potential of a semi-transparent photovoltaic double-skin facade in a cool-summer Mediterranean climate, Applied Energy 345–356doi:10.1016/j.apenergy.2015.12.074.

[19] A. Colsmann, A. Puetz, A. Bauer, J. Hanisch, E. Ahlswede, U. Lemmer, Efficient semi-transparent organic solar cells with good transparency color perception and rendering properties, Advanced Energy Materials 1 (4) (2011) 599–603. doi:10.1002/aenm.201000089.

[20] G. E. Eperon, V. M. Burlakov, A. Goriely, H. J. Snaith, Neutral color semitransparent microstructured perovskite solar cells, ACS Nano 8 (1) (2014) 591–598. doi:10.1021/nn4052309.

[21] K.-T. Lee, L. Guo, H. Park, Neutral- and Multi-Colored Semitransparent Perovskite Solar Cells, Molecules (4) 475. doi:10.3390/molecules21040475.

[22] P. G. O'Brien, A. Chutinan, P. Mahtani, K. Leong, G. a. Ozin, N. P. Kherani, Selectively transparent and conducting photonic crystal rear-contacts for thin-film silicon-based building integrated photovoltaics, Optics Express 19 (18) (2011) 17040. doi:10.1364/OE.19.017040.

[23] K.-S. Chen, J.-F. Salinas, H.-L. Yip, L. Huo, J. Hou, A. K.-Y. Jen, Semi-transparent polymer solar cells with 6% PCE, 25% average visible transmittance and a color rendering index close to 100 for power generating window applications, Energy & Environmental Science (11) 9551. doi:10.1039/c2ee22623e.

[24] A. Cannavale, M. Hörantner, G. E. Eperon, H. J. Snaith, F. Fiorito, U. Ayr, F. Martellotta, Building integration of semitransparent perovskite-based solar cells: Energy performance and visual comfort assessment, Applied Energy 94–107doi:10.1016/j.apenergy.2017.03.011.

[25] M. Saifullah, J. Gwak, J. H. Yun, Comprehensive review on material requirements, present status, and future prospects for building-integrated semitransparent photovoltaics (BISTPV), J. Mater. Chem. A 8512–8540doi:10.1039/C6TA01016D.

[26] Y. Zhao, G. A. Meek, B. G. Levine, R. R. Lunt, Near-infrared harvesting transparent luminescent solar concentrators, Advanced Optical Materials 2 (7) (2014) 606–611. doi:10.1002/adom.201400103.

[27] S. Xu, W. Liao, J. Huang, J. Kang, Optimal PV cell coverage ratio for semi-transparent photovoltaics on office building façades in central China, Energy and Buildings 130–138doi:10.1016/j.enbuild.2014.03.052.

[28] R. R. Lunt, V. Bulovic, Transparent, near-infrared organic photovoltaic

solar cells for window and energy-scavenging applications, Applied Physics Letters 98 (11). doi:10.1063/1.3567516.

[29] B. Cocilovo, A. Hashimura, D. J. Tweet, T. Voutsas, R. A. Norwood, Highly transparent light-harvesting window film, Applied Optics (30) 8990. doi:10.1364/AO.54.008990.

[30] M. Debije, Luminescent solar concentrators: Semiconductor solution, Nature Photonics (3) 143–144. doi:10.1038/nphoton.2017.20.

[31] V. I. Klimov, T. A. Baker, J. Lim, K. A. Velizhanin, H. McDaniel, Quality Factor of Luminescent Solar Concentrators and Practical Concentration Limits Attainable with Semiconductor Quantum Dots, ACS Photonics 3 (6) (2016) 1138–1148. doi:10.1021/acsphotonics.6b00307.

[32] M. G. Debije, Solar energy collectors with tunable transmission, Advanced Functional Materials 20 (9) (2010) 1498–1502. doi:10.1002/adfm.200902403.

[33] Y. Zhao, R. R. Lunt, Transparent luminescent solar concentrators for large-area solar windows enabled by massive stokes-shift nanocluster phosphors, Advanced Energy Materials 3 (9) (2013) 1143–1148. doi:10.1002/aenm.201300173.

[34] Y. Luo, L. Zhang, X. Wang, L. Xie, Z. Liu, J. Wu, Y. Zhang, X. He, A comparative study on thermal performance evaluation of a new double skin façade system integrated with photovoltaic blinds, Applied Energy 281–293doi:10.1016/j.apenergy.2017.05.026.

[35] Z. Hu, W. He, J. Ji, D. Hu, S. Lv, H. Chen, Z. Shen, Comparative study on the annual performance of three types of building integrated photovoltaic (BIPV) Trombe wall system, Applied Energy 81–93doi:10.1016/j.apenergy.2017.02.018.

[36] Z. Hu, W. He, D. Hu, S. Lv, L. Wang, J. Ji, H. Chen, J. Ma, Design, construction and performance testing of a PV blind-integrated Trombe wall module, Applied Energy 643–656doi:10.1016/j.apenergy.2017.06.078.

[37] T. Hong, C. Koo, J. Oh, K. Jeong, Nonlinearity analysis of the shading effect on the technical?economic performance of the building-integrated photovoltaic blind, Applied Energy 467–480doi:10.1016/j.apenergy.2016.05.027.

[38] H. S. Park, C. Koo, T. Hong, J. Oh, K. Jeong, A finite element model for estimating the techno-economic performance of the building-integrated photovoltaic blind, Applied Energy 211–227doi:10.1016/j.apenergy.2016.06.137.

[39] C. Koo, T. Hong, J. Oh, J.-K. Choi, Improving the prediction performance of the finite element model for estimating the technical performance of the distributed generation of solar power system in a building façade, Applied Energy (January) 41–53. doi:10.1016/j.apenergy.2018.01.081.

[40] W. Bahr, A comprehensive assessment methodology of the building integrated photovoltaic blind system, Energy and Buildings 703–708doi:10.1016/j.enbuild.2014.07.065.

[41] M. Radut, N. Bizon, Determining the power generated by the photovoltaic window blinds tilted at different angles for vertical & horizontal orientations, in: Proceedings of the 8th International Conference on Electronics, Computers and Artificial Intelligence, ECAI 2016, 2017, pp. 0–3. doi:10.1109/ECAI.2016.7861128.

[42] M. Mandalaki, T. Tsoutsos, N. Papamanolis, Integrated PV in shading systems for Mediterranean countries: Balance between energy production and visual comfort, Energy and Buildings 77 (2014) 445–456. doi:10.1016/j.enbuild.2014.03.046.

[43] S. Kang, T. Hwang, Theoretical analysis of the blinds integrated photovoltaic modules, Energy and Buildings 46 (2012) 86–91. doi:10.1016/j.enbuild.2011.10.042.

[44] S. Hong, A. S. Choi, M. Sung, Development and verification of a slat control method for a bi-directional PV blind, Applied Energy (June) 1321–1333. doi:10.1016/j.apenergy.2017.10.009.

[45] D. Rossi, Z. Nagy, A. Schlueter, Adaptive distributed robotics for environmental performance, occupant comfort and architectural expression, International Journal of Architectural Computing 10 (3) (2012) 341–359.

[46] J. Hofer, A. Groenewolt, P. Jayathissa, Z. Nagy, A. Schlueter, Parametric analysis and systems design of dynamic photovoltaic shading modules, Energy Science & Engineering n/a–n/adoi:10.1002/ese3.115.

[47] P. Jayathissa, M. Luzzatto, J. Schmidli, J. Hofer, Z. Nagy, A. Schlueter, Optimising building net energy demand with dynamic BIPV shading, Applied Energy 726–735doi:10.1016/j.apenergy.2017.05.083.

[48] H. Mousazadeh, A. Keyhani, A. Javadi, H. Mobli, K. Abrinia, A. Sharifi, A review of principle and sun-tracking methods for maximizing solar systems output, Renewable and Sustainable Energy Reviews 13 (8) (2009) 1800–1818. doi:10.1016/j.rser.2009.01.022.

[49] C. A. Gueymard, Direct and indirect uncertainties in the prediction of tilted irradiance for solar engineering applications, Solar Energy (3) 432–444. doi:10.1016/j.solener.2008.11.004.

[50] A. Smets, K. Jäger, O. Isabella, R. van Swaaij, M. Zeman, Solar Energy: The Physics and Engineering of Photovoltaic Conversion, Technologies and Systems, UIT Cambridge.

[51] A. Chopra, Introduction to google sketchup, John Wiley & Sons, 2012.

[52] Y. Gao, J. Dong, O. Isabella, M. Zeman, G. Q. Zhang, Daylighting Simulation and Analysis of Buildings with Dynamic Photovoltaic Window Shading Elements, Vol. 1, 2017, pp. 52–55.

[53] I. Reda, A. Andreas, Solar position algorithm for solar radiation applications (2004). doi:10.1016/j.solener.2003.12.003.

[54] S. Dongaonkar, M. A. Alam, Geometrical design of thin film photovoltaic modules for improved shade tolerance and performance, Progress in Photovoltaics: Research and Applications 23 (2) (2015) 170–181. arXiv:1303.4604, doi:10.1002/pip.2410.

[55] K. Ishaque, Z. Salam, Syafaruddin, A comprehensive MATLAB Simulink PV system simulator with partial shading capability based on two-diode model, Solar Energy 85 (9) (2011) 2217–2227. doi:10.1016/j.solener.2011.06.008.

[56] I. Konstantzos, A. Tzempelikos, Daylight Glare Probability Measurements And Correlation With Indoor Illuminances In A Full- Scale Office With Dynamic Shading Controls, International High Performance Buildings Conference 147.